BOSTON UNIVERSITY

GRADUATE SCHOOL OF ARTS AND SCIENCES

Dissertation

# MEASUREMENT OF THE ANOMALOUS MAGNETIC MOMENT OF THE POSITIVE MUON TO .SOMETHING PARTS PER BILLION

by

**NICHOLAS BRENNAN KINNAIRD**

B.S., University of Texas at Austin, 2013
B.S., University of Texas at Austin, 2013
M.A., Boston University, 2016

Submitted in partial fulfillment of the

requirements for the degree of

Doctor of Philosophy

2019

Approved by

First Reader

B. L. Roberts, PhD
Professor of Physics

Second Reader

R. M. Carey, PhD
Professor of Physics

Third Reader

J. P. Miller, PhD
Professor of Physics

## Dedication

I dedicate this thesis to

## Acknowledgments

Here go all your acknowledgments. You know, your advisor, funding agency, lab mates, etc., and of course your family.

As for me, I would like to thank Jonathan Polimeni for cleaning up old LaTeX style files and templates so that Engineering students would not have to suffer typesetting dissertations in MS Word. Also, I would like to thank IDS/ISS group (ECE) and CV/CNS lab graduates for their contributions and tweaks to this scheme over the years (after many frustrations when preparing their final document for BU library). In particular, I would like to thank Limor Martin who has helped with the transition to PDF-only dissertation format (no more printing hardcopies – hooray !!!)

The stylistic and aesthetic conventions implemented in this LaTeX thesis/dissertation format would not have been possible without the help from Brendan McDermot of Mugar library and Martha Wellman of CAS.

Finally, credit is due to Stephen Gildea for the MIT style file off which this current version is based, and Paolo Gaudiano for porting the MIT style to one compatible with BU requirements.

Janusz Konrad

Professor

ECE Department

# MEASUREMENT OF THE ANOMALOUS MAGNETIC MOMENT OF THE POSITIVE MUON TO .SOMETHING PARTS PER BILLION

(Order No. )

**NICHOLAS BRENNAN KINNAIRD**

Boston University, Graduate School of Arts and Sciences, 2019

Major Professor: B. L. Roberts, Professor of Physics

ABSTRACT

Have you ever wondered why this is called an *abstract*? Weird thing is that its legal to cite the abstract of a dissertation alone, apart from the rest of the manuscript.

# Contents

# List of Tables

# List of Figures

# List of Abbreviations

| | | |
|---|---|---|
| BNL | ............. | Brookhaven National Laboratory |
| BSM | ............. | beyond the standard model |
| CBO | ............. | coherent betatron oscillation |
| E821 | ............. | Brookhaven Muon $g - 2$ Experiment |
| E989 | ............. | Fermilab Muon $g - 2$ Experiment |
| EW | ............. | electroweak |
| FNAL | ............. | Fermi National Accelerator Laboratory |
| Geane | ............. | Geometry and Error Propagation |
| Geant4 | ............. | Geometry and Tracking 4 |
| IBMS | ............. | inflector beam monitoring system |
| PMT | ............. | photo-multiplier tube |
| ppb | ............. | parts per billion |
| ppm | ............. | parts per million |
| ppt | ............. | parts per trillion |
| QCD | ............. | quantum chromodynamics |
| QED | ............. | quantum electrodynamics |
| SiPM | ............. | silicon photo-multiplier |
| SM | ............. | Standard Model |
| WFD | ............. | waveform digitizer |

# Chapter 1

# Introduction

The prevailing theory for particle physics, the Standard Model (SM), has had tremendous success in describing our universe. It has been used to predict and explain a wide variety of phenomena, particles, properties, and interactions to great precision. However, in spite of its success in explaining nearly all experimental results, there remain unanswered questions about our universe. Some of these include the matter-antimatter asymmetry, the source of mass for the neutrinos, the existence of dark matter, and an inability to fully incorporate our best theory of gravitation. Many particle physics experiments around the world are being devised and conducted in order to shed light on these questions and improve our understanding of reality. One such particular experiment is the Fermilab Muon $g-2$ Experiment (E989) underway at the Fermi National Accelerator Laboratory (FNAL) located in Batavia, Illinois.

I have been a part of the E989 experiment since I began my graduate degree six years ago. Three years ago I moved from Boston to Batavia to get more involved by being where the action is. This dissertation will describe the E989 experiment and the work which I have done for it along the way in detail. Chapter 1 will provide experimental and theoretical background to the experiment, as well its motivation. Chapter 2 will describe the experimental principle. Chapter 3 will describe the magnetic field portion of the experiment, and magnetic field simulations I conducted. Chapter 4 will describe the straw tracking detectors and their measurements, including the track fitting I wrote. Chapter 5 will describe the frequency measurement portion of the experiment, and detail my analysis results from data taken in the first half of 2018. Finally, Chapter 6 will concluded the thesis and the results contained within.

## 1.1 Magnetic Moments of Particles

In order to understand the purpose of the Fermilab Muon $g-2$ Experiment, first we need to understand what the $g$ in $g-2$ is. This is what the experiment is measuring. All particles have intrinsic properties. One of those properties is the magnetic dipole moment.[1] This property of a particle is related to its spin through the equation

$$\vec{\mu} = g\frac{q}{2m}\vec{s}, \tag{1.1}$$

where $\vec{\mu}$ is the magnetic dipole moment of a particle, $\vec{s}$ is its spin vector, $m$ is its mass, $q = \pm e$ where $e$ is the elementary charge, and $g$ is the so called "g-factor". $g$ is some measureable and predictable constant, which as shown in Equation 1.1 relates the magnetic moment of a particle to its spin angular momentum. Since the torque on a particle in a magnetic field is

$$\vec{N} = \vec{\mu} \times \vec{B}, \tag{1.2}$$

the rate at which a particles spin precesses in a magnetic field will depend on $g$. This happens to be one of the key physics principles in the E989 experiment as will be discussed later.

In a Dirac theory, $g$ is equal to 2 for spin-1/2 particles with no internal structure [1]. See Appendix A for a nice derivation of this result. It turns out however, that $g$ is not quite equal to 2 even for these types of particles. Motivated by early experimental discrepencies such as the measurements of the hyperfine structure in hydrogen [2],

[1] *Magnetic dipole moment* and *magnetic moment* are equivalent when talking about particles.

in 1948 Schwinger calculated the first "radiative correction" to the electron magnetic moment [3]. In a quantum field theory, interactions of the particle with virtual particles in loops will contribute to the value of $g$. In this context it is nicer to recast the magnetic dipole moment formula as

$$\begin{aligned} \vec{\mu} &= 2(1+a)\frac{q}{2m}\vec{s}, \\ a &= \frac{g-2}{2}, \end{aligned} \tag{1.3}$$

where $a$ is called the "anamolous" part of the magnetic moment, and contains all higher order corrections. The first correction calculated to $a$ by Schwinger was $a = \alpha/2\pi \approx 0.00116$, where $\alpha$ is the fine structure constant. By measuring $a$, the SM theory can be tested and extensions to it constrained. The measurement of the anamolous piece of the muon is indeed where the Fermilab Muon $g-2$ Experiment gets its name.

## 1.2 Standard Model Contributions to $a_\mu$

(Double check all numbers and make sure the correlations in the final result are considered appropriately. Make sure latest theoretical results are included.)

Before experimental results have any real meaning, they need a theory with which to compare. The latest theoretical predictions for the muon magnetic moment will be presented here. The contributions to $a_\mu$ can be summed from separate pieces relating to different parts of the SM. These include the quantum-electrodynamics (QED) corrections purely from other leptons and photons, the electroweak (EW) corrections from interactions with the weak force bosons $W^\pm$ and $Z^0$, and the hadronic corrections from interactions with hadrons:

$$a_\mu^{\mathrm{SM}} = a_\mu^{\mathrm{QED}} + a_\mu^{\mathrm{EW}} + a_\mu^{\mathrm{Had}} \tag{1.4}$$

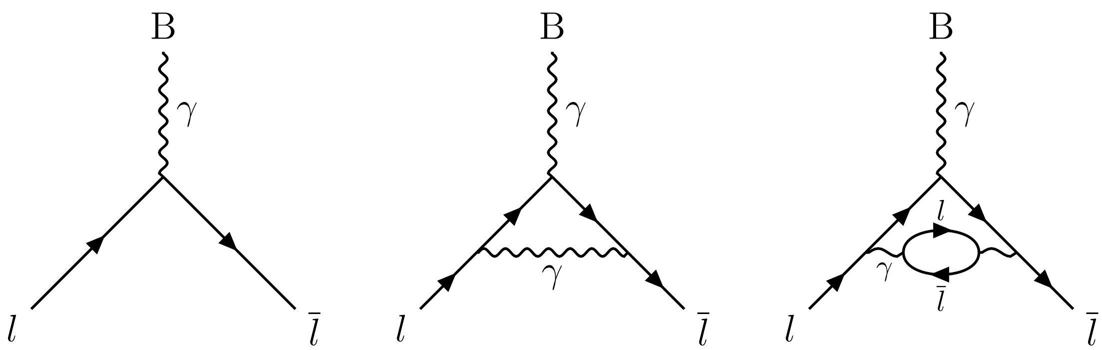


(a) Dirac result, $g = 2$.

(b) The first loop diagram, calculated by Schwinger.

(c) A two loop diagram.

Figure 1·1: The first of many QED diagrams contributing to $a$. B is an external magnetic field. Feynman diagrams made with [6, 7].

### 1.2.1 QED

The QED contributions to $a_\mu$ stem solely from loops with virtual leptons and photons. They are very well understood and have been calculated to very high order, having been calculated up to five loop level from over 12,000 Feynman diagrams [4, 5]. This has been done either analytically or numerically. The first couple of diagrams including the Dirac $g = 2$ and Schwinger diagrams are shown in Figure 1·1. The value is

$$\begin{aligned} a_\mu^{\mathrm{QED}} &= \sum_{n=1}^{\infty} C_n \left(\frac{\alpha}{\pi}\right)^n, \\ &= (11658471.8971 \pm 0.007) \times 10^{10}, \end{aligned} \tag{1.5}$$

where in the first line $a_\mu^{\mathrm{QED}}$ is expressed as a perturbative expansion of the fine structure constant. $C_1 = 1/2$ is the Schwinger result mentioned previously stemming from the diagram shown in Figure 1·1b. Over 99% of the value of $a_\mu$ comes from the QED sector, but the error is much smaller than the other contributions, as well as the experimental uncertainty.

### 1.2.2 Electroweak

The electroweak contributions to $a_\mu$ are known to two loop level, with some three loop parts estimated. The contributions stem from couplings with the heavy weak gauge bosons. The different one loop diagrams and an example two loop diagram are shown in Figure 1·2. Per usual Feynman rules, the propagators will contain the masses of the interacting bosons, while the kinematics will contain the masses of the leptons. For calculations of a muon in the case of Figure 1·2a, these result in a factor $\sim (m_\mu/m_{Z^0})^2$. Because the mass of the gauge bosons are so much more than the muon, these processes are necessarily suppressed and the electroweak contributions to $a_\mu$ are small. For this reason knowing these contributions only up to two loop level is sufficient. The value of the electroweak contributions is

$$a_\mu^{\mathrm{EW}} = (15.12 \pm 0.01) \times 10^{10}, \tag{1.6}$$

with improvements having been made recently [8, 9]. Again the error on these contibutions is small compared to the hadronic contributions discussed next, as well as the experimental uncertainty.

### 1.2.3 Hadronic

The hadronic contributions to $a_\mu$ stem from interactions with hadrons. Because they cannot be calculated perturbatively at low energies due to the QCD nature of these particles, these calculations comprise the dominant uncertainty in the SM calculation. This makes their error estimation extra important when comparing to experiment. Most active work on the theoretical side of things is in this sector. These contributions can be separated into two parts

$$a_\mu^{\mathrm{Had}} = a_\mu^{\mathrm{HVP}} + a_\mu^{\mathrm{HLbL}}. \tag{1.7}$$

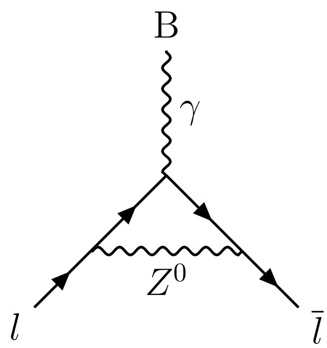


(a) Exchange of a virtual $Z^0$ boson.

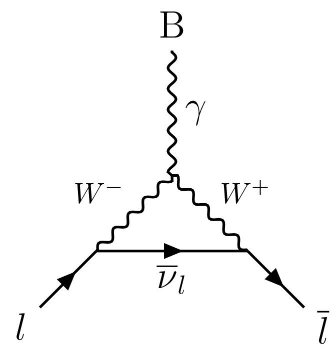


(b) Electroweak loop with $W$ bosons.

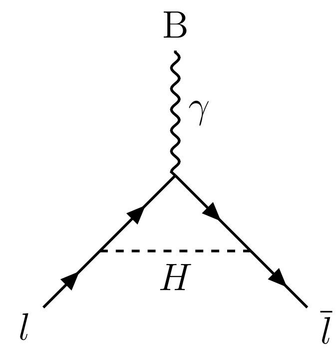


(c) Exchange of a Higgs boson.

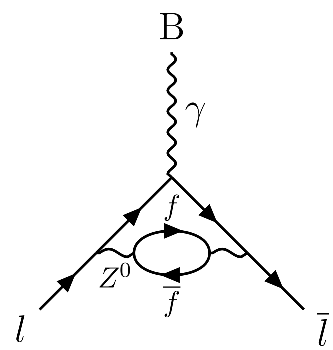


(d) Second order electroweak diagram.

Figure 1·2: First order (and one second) weak diagrams contributing to $a$. B is an external magnetic field. Feynman diagrams made with [6, 7].

**Hadronic Vacuum Polarization**

The first of these hadronic contribution parts is the hadronic vacuum polarization part (HVP), the first order diagram of which is shown in Figure 1·3a. There are two main prescriptions for calculating these contributions. The first is to use a dispersive approach to introduce a virtual hadron blob into the integral calculation for the photon propagator [10], and then utilize the optical theorem to relate the imaginary part of that propagator to the total cross-section of electron-positron annihilation to hadrons. While this could be solved perturbatively for a lepton blob in place of the hadron blob, this is instead a data driven approach when considering non-perturbative QCD. The details of dispersion theory will not be described here. The leading order contribution can be written as

$$a_\mu^{\mathrm{HVP;LO}} = \left(\frac{\alpha m_\mu}{3\pi}\right)^2 \int_{m_\pi^2}^{\infty} \frac{ds}{s^2} K(s) R(s) \tag{1.8}$$

where $K(s)$ is some kinematic factor, and $R(s)$ is a ratio of cross-sections

$$R(s) = \frac{\sigma(e^+e^- \to \mathrm{hadrons})}{\sigma(e^+e^- \to \mu^+\mu^-)}. \tag{1.9}$$

The cross-section data for this relation has been measured in parts by various experiments, including KLOE, CLEO, BaBar, and BESIII [11, 12, 13, 14]. The analysis by Keshavarzi et al. [15] gives results as

$$\begin{aligned} a_\mu^{\mathrm{HVP;LO}} &= (693.26 \pm 2.46) \times 10^{10}, \\ a_\mu^{\mathrm{HVP;NLO}} &= (-9.82 \pm 0.04) \times 10^{10}, \end{aligned} \tag{1.10}$$

where $a_\mu^{\mathrm{HVP;NLO}}$ is the next to leading order calculation. This calculation is consistent with Davier et al. [16]. In this way, the SM theory has some dependence on experimental results. This is acceptable as the experimental measurements are

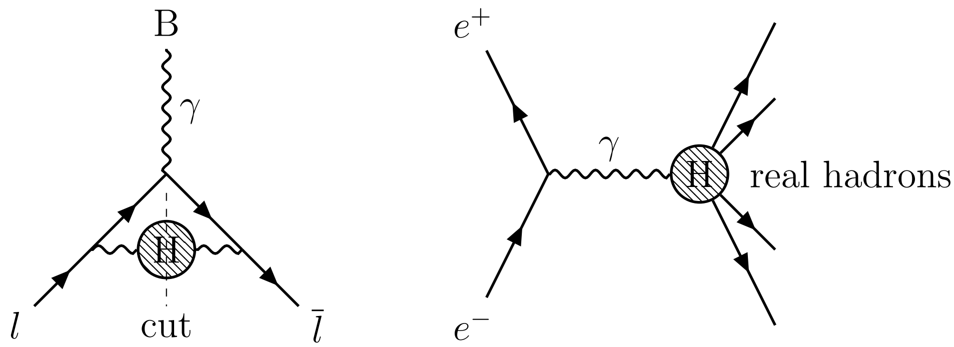


(a) The first order HVP diagram. The blob H in the middle indicates any combination of hadrons which satisfy the Feynman rules.

(b) The Feynman diagram for electron positron annihilation to hadrons.

Figure 1·3: The first order HVP diagram on the left, which can be related to the diagram on the right by making a 'cut' across the virtual hadrons blob. B is an external magnetic field. Feynman diagrams made with [6, 7].

straightforward observables.

The second prescription to estimating the HVP contributions is a first principles approach, using lattice QCD and QED. It is a gauge theory defined on a matrix of points in time and space. Once the matrix is taken infinitely large with the spacing between the points infinitely small, the behavior from a continuous theory is recovered. The results for the leading order estimates of $a_\mu^{\mathrm{HVP;LO}}$ are consistent with those provided above, though the error is larger. If the calculation is supplemented with the cross-section data described above, then this method provides the most precise determination of $a_\mu^{\mathrm{HVP;LO}}$ [17].

### Hadronic Light-by-Light

The second of these hadronic contribution parts is a higher order four photon interaction, termed hadronic light-by-light. Diagrams are are shown in Figure 1·4. Again perturbation theory is unable to assist in the calculation of these contributions. For a

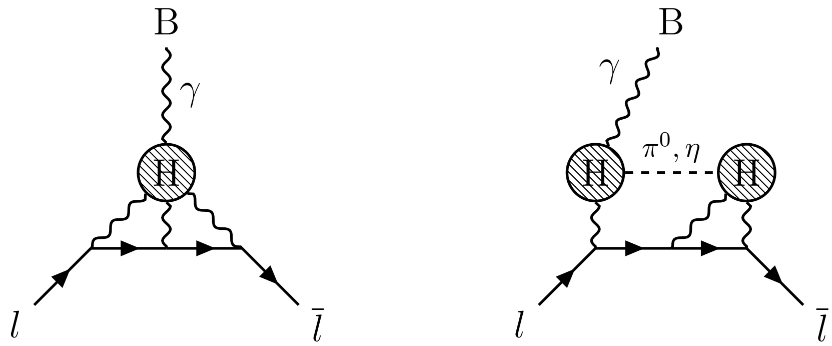


(a) The first HLbL diagram, where three photons are exchanged with some virtual hadrons blob.

(b) A second HLbL diagram, where three photons are exchanged with two virtual hadrons blobs, that are connected with some virtual chargeless propagator.

Figure 1·4: HLbL diagrams contributing to $a_\mu$. B is an external magnetic field. Feynman diagrams made with [6, 7].

long time the calculation of these diagrams was model dependent, and has therefore been the most contentious part of the SM calculation. In more recent years, there have been efforts to produce results using dispersive and lattice approaches [18]. In accordance with all of this, the error on this contribution is large, comparable to that of the $a_\mu^{\text{HVP;LO}}$ term, even though the size of this contribution is small. The value of the HLbL contributions to $a_\mu$ quoted by Keshavarzi et al. [15] is

$$a_\mu^{\text{HLbL}} = (9.8 \pm 2.6) \times 10^{10}. \tag{1.11}$$

### 1.2.4 Combined Standard Model Value

The sum of the $a_\mu$ contributions listed here is

$$\begin{aligned} a_\mu^{\text{SM}} &= a_\mu^{\text{QED}} + a_\mu^{\text{EW}} + a_\mu^{\text{Had}}, \\ &= (11659180.26 \pm 3.58) \times 10^{10}. \end{aligned} \tag{1.12}$$

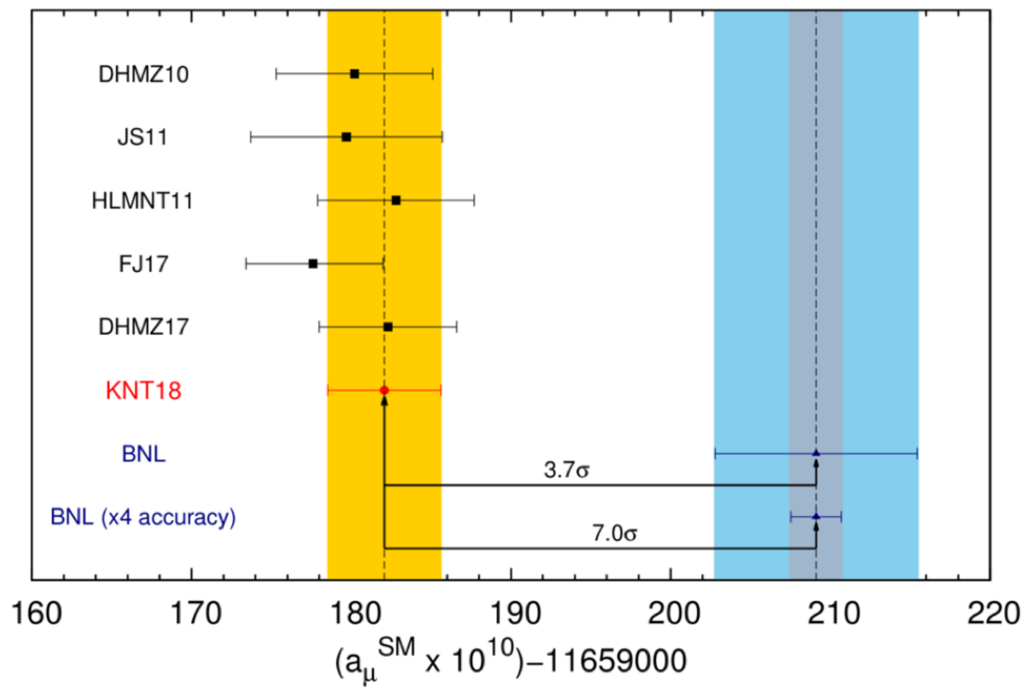


Figure 1·5: Various theoretical values for $a_\mu$ on the left, as compared to the most recent and extrapolated experimental result on the right. Plot courtesy of Alex Keshavarzi [15].

The relative uncertainty of this result is 307 ppb. Other analyses with different values for the various contributions typically agree well, as shown on the left side of Figure 1·5. Depending on what calculations are used, the discrepancy between theory and experiment ranges from 3-4 $\sigma$. The latest experimental result is described in the following section.

## 1.3 Experimental Value of $a_\mu$ and Discrepancy with $a_\mu^{\mathrm{SM}}$

The theoretical contributions to $a_\mu$ listed in the previous sections have improved over time as methods have matured and more experimental data gathered. Similarly, work on the direct experimental measurement of $a_\mu$ has been going on for decades, with more precise results being determined over time [19]. The most recent experiment to measure $g-2$ was the Brookhaven Muon $g-2$ Experiment (E821) held at Brookhaven National Laboratory (BNL) in 2001 [20]. That experiment measured a value for $a_\mu$ of

$$a_\mu^{\text{Exp}} = (11659208.0 \pm 6.3) \times 10^{10}, \tag{1.13}$$

which corresponds to a 540 ppb relative uncertainty. Note that the uncertainty of the experimental measurement is comparable to that of the theory, necessitating precise understanding of all the different theoretical parts. The difference between the experimental and theoretical values here is

$$a_\mu^{\text{Exp}} - a_\mu^{\text{SM}} = (27.74 \pm 7.25) \times 10^{10}, \tag{1.14}$$

corresponding to a discrepancy of $3.83\sigma$ from 0.

-double check the numbers here later on down the line, values like $a_\mu$ experimental may even have changed if other constants have changed

## 1.4 Beyond the Standard Model and the Purpose of E989

While the discrepancy between experiment and theory might be attributed to miscalculations in the theory or systematic errors in the E821 experiment, no such errors have been found despite serious attempts to resolve the two. Indeed the discrepancy has only grown over time as the theoretical calculations have matured. The most intriguing and exciting source of the discrepancy would be physics beyond the standard model (BSM). Since the value of $a_\mu$ receives contributions from all particles that couple to the muon through virtual loops, unknown particles might be the source of this discrepancy. Specifically, since the contribution to the magnetic moment from

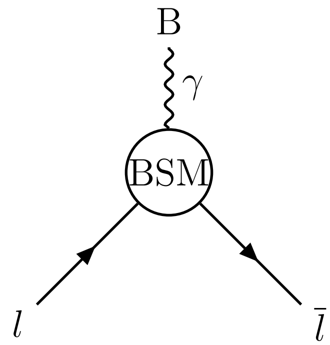


Figure 1·6: An example Feynman diagram, where the leptons couple to an external magnetic field B through some BSM physics. Feynman diagrams made with [6, 7].

heavy virtual particles goes as

$$a \sim \frac{m^2}{\Lambda^2}, \tag{1.15}$$

where $\Lambda$ is the mass scale of the new particle and m the mass of the lepton in question, the senstivity of the muon as compared to the electron to large mass scales is $m_\mu^2/m_e^2 \approx$ 43000 greater. It is possible from this reason that even though the magnetic moment of the electron has been measured extraordinarily precisely, to .28 parts per trillion (ppt) [21], it has provided no indication of anything new, whereas the magnetic moment of the muon might provide definitive evidence of new phyiscs.

A basic example diagram of new physics is shown in Figure 1·6. Because the discrepancy from the previous experiment was not at the $5\sigma$ level necessary to classify it as a discovery, the E989 experiment was undertaken. Indeed with the lack of new physics results coming out of the LHC and other experiments, E989 is especially positioned to uncover something new at a time where there are so few hints of new physics. Because of this, the interest in the E821 experiment and underway E989 experiment has only grown over time. The number of citations for the E821 results has been consistently high over the years and is shown in Figure 1·7.

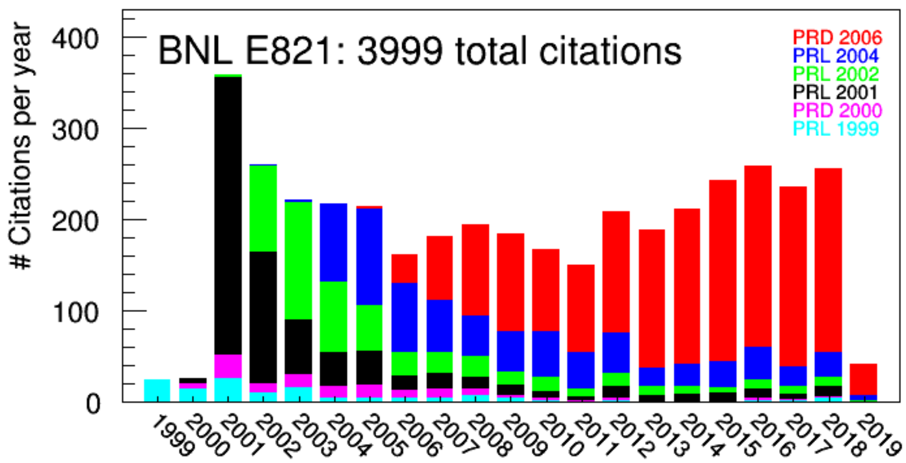


Figure 1·7: The number of citations for the BNL experiment publications as a function of year. Plot courtesy of Lee Roberts.

The E989 experiment has the goal of measuring $a_\mu$ to 140 ppb over the course of several years. This would be a factor of 4 improvement over the E821 result stemming from a 20 times increase in statistics, which was the limiter in the previous experiment. Assuming the same value for $a_\mu$ is measured, this would push the discrepancy over the $5\sigma$ mark to approximately $7\sigma$, as shown in Figure 1·5. The data comprising Run 1, gathered in the spring and summer of 2018, is the subject of this thesis, and corresponds to an experimental uncertainty comparable to the E821 result. When it's all said and done, the hope is that we measure something new and exciting, pushing the discrepancy out beyond the $5\sigma$ level. Even if we do not however, it is valuable in itself to resolve this theoretical and experimental conflict.

# Chapter 2

# Principle Technique of E989

As referenced in Equation 1.2, a particle in a magnetic field will experience a torque which attempts to line up the magnetic dipole moment of the particle with the external field. Because of this, in a dipole field a particles spin will turn at the Larmour precesssion frequency [22]

$$\vec{\omega}_s = -g\frac{q}{2m}\vec{B} - (1-\gamma)\frac{q}{\gamma m}\vec{B}, \tag{2.1}$$

where as before $m$ is the particles mass, $q = \pm e$ where $e$ is the elementary charge, $g$ is the g-factor, $\gamma$ is the Lorentz relativistic factor, and $B$ is an external magnetic field. The second term is a relativistic correction to the precession frequency called Thomas precession [22]. Similarly, a particle with some momentum will orbit at the cyclotron frequency

$$\vec{\omega}_c = -\frac{q}{\gamma m}\vec{B}. \tag{2.2}$$

By taking the difference between these two frequencies we arrive at the "spin difference frequency"

$$\vec{\omega}_a = \vec{\omega}_s - \vec{\omega}_c = -\frac{g-2}{2}\frac{q}{m}\vec{B} = -a\frac{q}{m}\vec{B}, \tag{2.3}$$

a frequency that is directly proportional to the anomalous magnetic moment $a$. Briefly note that if $g = 2$ as in a Dirac theory, then the particles spin would turn at the same rate as the momentum vector, and this spin difference frequency $\omega_a$ would be identically 0. If this spin difference frequency for a muon and the external magnetic dipole field can be measured, then the anomalous magnetic moment of the muon $a_\mu$ can be measured. Introductory descriptions for both will be given here, while the details are left to Chapter 5 and Chapter 3 respectively.

## 2.1 Measuring $\omega_a$

How can $\omega_a$ for muons be measured? The answer lies with two key points in the dynamics of muon decay. Positive muons decay to a positron and two neutrinos, as shown in Figure 2·1a. The first point is that because of the parity violating nature of the weak interaction, the decay positron will be preferentially emitted right-handed, with its spin directed in the same direction as its momentum [23]. The second key point is that angular momentum must be conserved. Consider the most extreme examples of maximum and minimum energy positrons as shown in Figure 2·2. In the muon rest frame, decay positrons with maximum energy will be emitted opposite to the two neutrinos. Since neutrinos and anti-neutrinos must be left and right-handed respectively, thus having their spins anti-parallel and parallel to their momentum, by the law of conservation of angular momentum the positron must have its spin be parallel to the spin of the muon at the time of the decay. By the opposite argument, decay positrons emitted with minimum energy such that the neutrinos are ejected opposite to one another must have their spins be anti-parallel to that of the muon at the time of decay. These two points combined together means that higher energy decay postrons will preferentially be emitted in directions parallel to the muon spin at the time of decay, while lower energy decay positrons will preferentially be emitted in directions anti-parallel to the muon spin at the time of the decay.

This correlation between the emitted direction of the decay positron and the

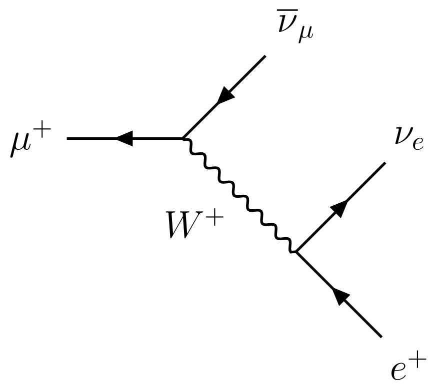


(a) $\mu^+$ decay through a $W^+$ boson to a positron, muon anti-neutrino, and an electron neutrino. This is the dominant decay mode.

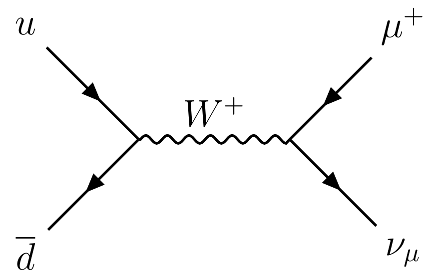


(b) $\pi^+$ decay through a $W^+$ boson to a $\mu^+$.

Figure 2·1: Feynman diagrams for muon (left) and pion (right) decay.

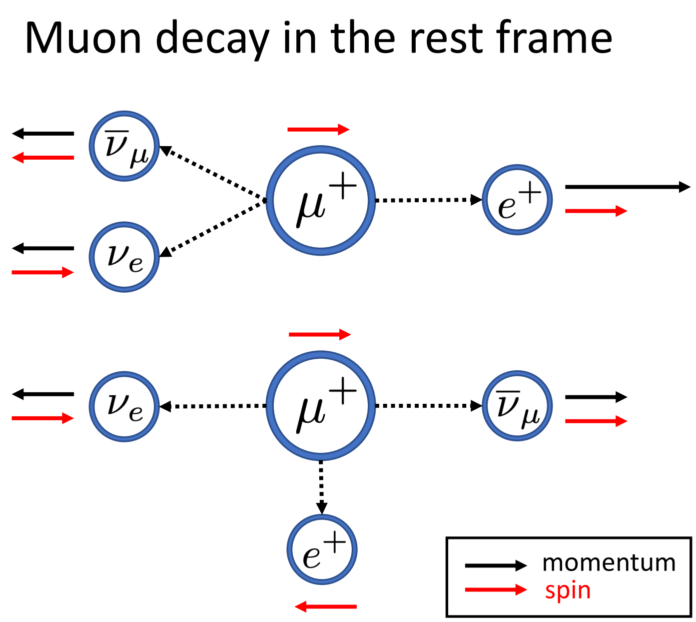


Figure 2·2: Muon decay pictures for maximum and minimum energy decay positrons. Due to the conservation of angular momentum and the single possible helicity states of the decay neutrinos, the spin of the decay positron is exactly parallel to the spin of the muon at the time of the decay for maximum energy decay positrons (top), or anti-parallel for minimum energy decay positrons (bottom).

spin of the muon is the signature needed to measure $\omega_a$. By placing an ensemble of polarized muons within a magnetic storage ring, those muons will orbit at the cyclotron frequency and their spins will precess at the Larmour frequency. As they go around the ring they will decay to positrons whose energy and decay directions contain information about the spin of the muon.

The differential decay distribution in the muon rest frame is described by [23]

$$dP(y,\theta) \propto N(y)[1 \pm A(y)\cos(\theta)]dyd\Omega, \tag{2.4}$$

where $y = E/E_{max}$ is the energy fraction of the positron, $N(y)$ is the number distribution of decay positrons, $A(y)$ is the so called asymmetry encoding the preferred direction, $\theta$ is the angle between the spin of the muon and the momentum of the positron $\cos^{-1}(\hat{p}\cdot\hat{s})$, and the $\pm$ stands for the positive and negative muon respectively. Here the energy of the positron is assumed to be much greater than its mass. The number distribution and asymmetry are given by [23]

$$\begin{aligned} N(y) &= 2y^2(3-2y^2), \\ A(y) &= \frac{2y-1}{3-2y}, \end{aligned} \tag{2.5}$$

and are shown in Figure 2·3a.

Specifically, the number of positrons emitted in the forward direction above some energy threshold will be modulated by $\omega_a$

Specifically, the positrons emitted in the forward direction will be modulated by $\omega_a$ as the muon spins precess about the momentum vector

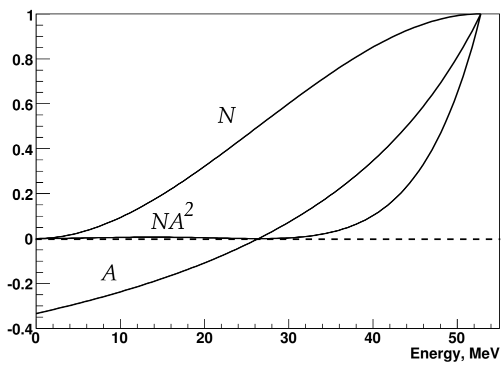


(a) Muon rest frame

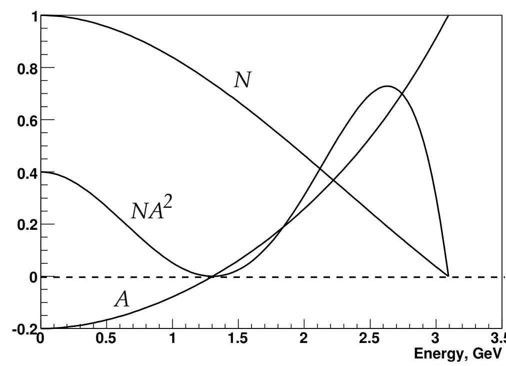


(b) Lab frame

Figure 2·3: Decay number distribution and asymmetry in the muon rest frame (left) and in the lab frame (right) for a maximum positron energy of 3.1 GeV.

In the presence of an electric field, which is useful in storing the muon beam within a dipole magnetic field, this expands to

$$\vec{\omega}_a = -\frac{Qe}{m}[a_\mu \vec{B} - (a_\mu - \frac{1}{\gamma^2 - 1})(\vec{\beta} \times \vec{E})], \tag{2.6}$$

where now the measurable quanties are vector quantities. Finally, for realistic cases of muon momentum which is non-orthogonal to the magnetic field, the spin difference frequency becomes

$$\vec{\omega}_a = -\frac{Qe}{m}[a_\mu \vec{B} - a_\mu(\frac{\gamma}{\gamma + 1})(\vec{\beta} \cdot \vec{B})\vec{B} - (a_\mu - \frac{1}{\gamma^2 - 1})(\vec{\beta} \times \vec{E})]. \tag{2.7}$$

If the motion of the muons is largely perpendicular to the magnetic field, then the second term is small and can be corrected for. If the particles have a momentum of approximately 3.09 GeV/c, the so called "magic momentum," then the third term is small and can be corrected for. These will be talked about later.

In order to measure the spin difference frequency of the muon, a clever technique is used. Decay muons in the pion rest frame are 100% polarized due to conservation of angular momentum and the fact that the decay neutrino must have a specific helicity. Within a pion beam then the highest and lowest energy decay muons are polarized. Muons will decay to positrons with a lifetime of about 2.2 $\mu$s, and the positrons with the highest energies will be correlated with the muon spin, a so called "self-analyzing" decay. The single available decay state for a maximum energy positron illustrates this in Figure **??**. Thus, by aquiring a large sample of polarized muons and injecting them into a storage ring

-explain the physics -explain how we get at the physics with our ring and detectors -parity violation -actually write out the decay states before explaining some things - well shouldn't these have been talked about before?? maybe not -decay probabilities and all that -don't measure all decay positrons -By injecting a large ensemble of

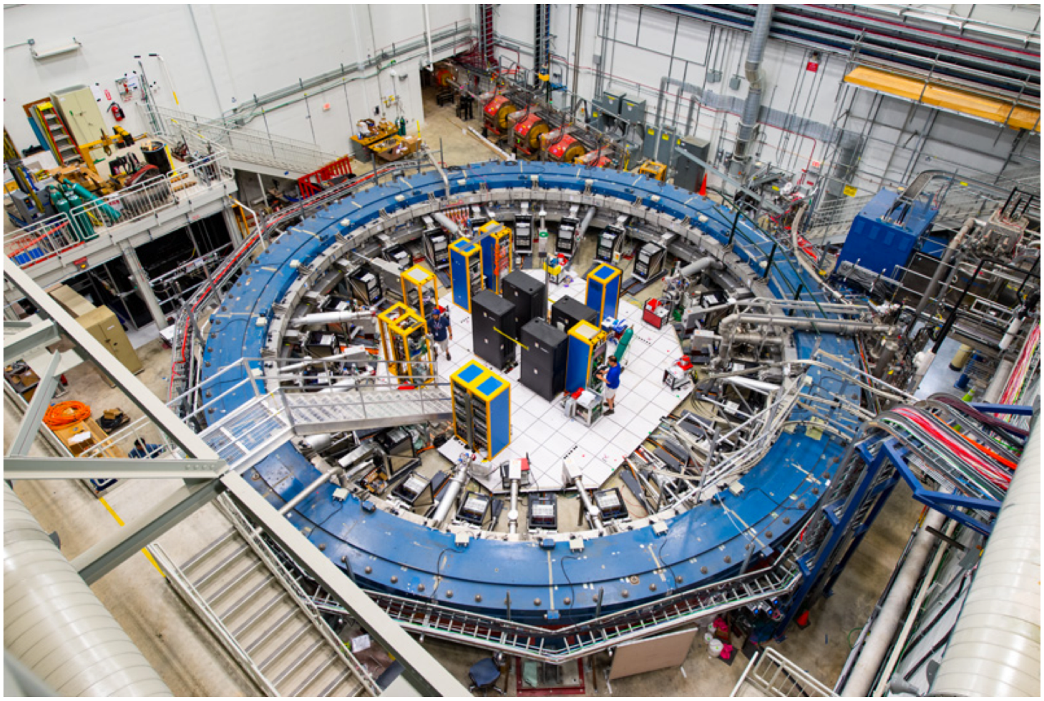

Figure 2·4: clean up and possibly replace

muons and -by measuring a subset of ensemble of muons.... -Careful with spin vs polarization

## 2.2 Measuring B

## 2.3 Accelerator

[24]

## 2.4 Injection

the inflector

## 2.5 Storage

kickers and quads

# Chapter 3

# Magnetic Field Measurement

## 3.1 Trolley

## 3.2 Opera Simulations

Where does this section really go?

# Chapter 4

# Straw Tracking Analysis

## 4.1 Straw Tracking Intro

As was talked about briefly in section **??**, the straw trackers are used to provide information about the muon beam, as well as info for the calorimeters. The straw track reconstruction is performed in several stages. The “Track Finding” stage takes incoming hits and decides which hits should be grouped together to form a single track for a single positron. The “Track Fitting” stage fits the measured positions of these invididivual hits and forms a single track describing the trajectory of the incident positron. Finally the “Track Extrapolation” stage takes the fitted track information and extrapolates the position and momentum components to the regions of interest, namely the storage region and the calorimeter.

-see the previous section for the hardware information... -Geane (Geometry and Error Propagation)

## 4.2 Track Finding

## 4.3 Track Fitting

The Geane fitting routines originated in Fortran with the EMC collaboration, and was used in the precursor E821 experiment as well as the PANDA experiment with some success [25], [26]. (I’m not actually aware of a useful reference for it’s use in E821, and there are some other instances of its use as well in other experiments. In E821

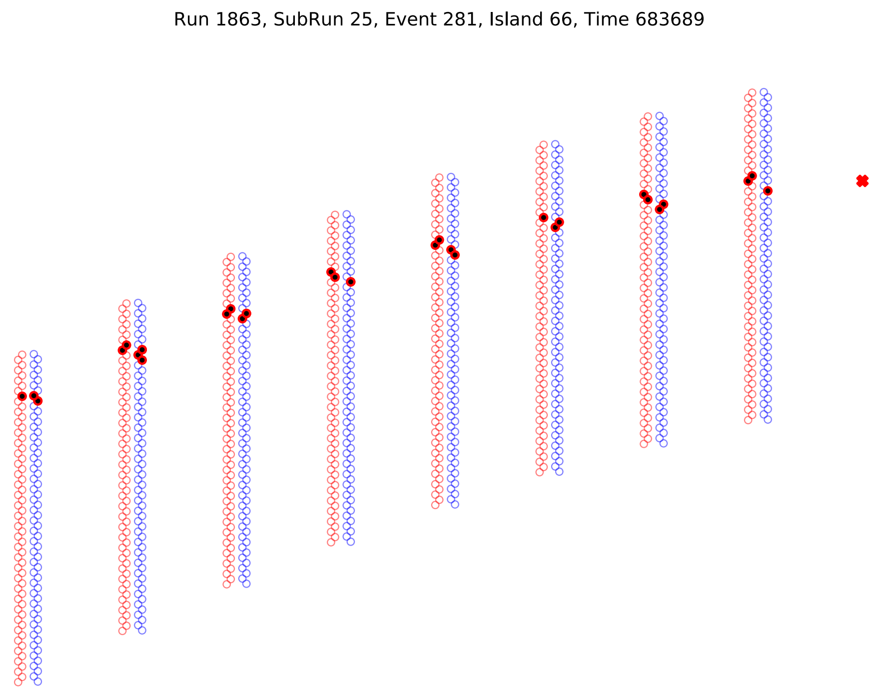


Figure 4·1: clean up and possibly replace

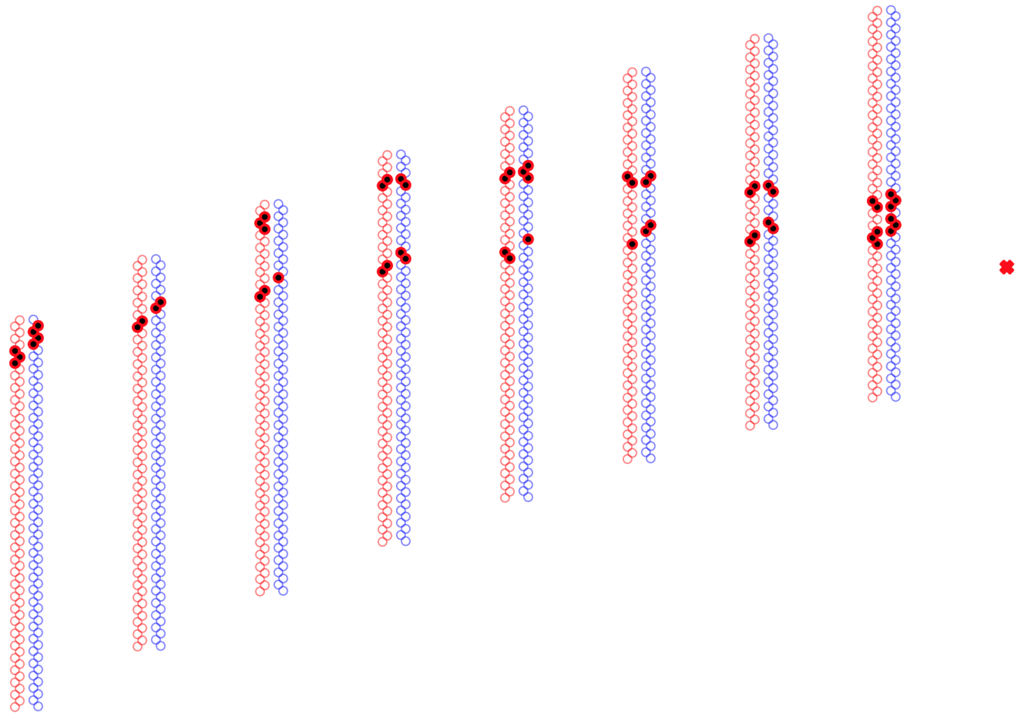

Figure 4·2: clean up and possibly replace

there was a single tracking chamber which was never put to full use.) The core error propagation routines were at some point added to Geant4 under the error_propagation directory which is included in all default installs. The tracking code strengths lie with its direct implementation and access to the Geant4 geometry and field, and its ability to handle the field inhomogeneties. The Geane fitting algorithm code which makes use of the Geant4 error propagation routines follows the structure of [25] and is detailed in the Formalism section in this paper. It is a relatively straight forward least squares global $\chi^2$ minimization algorithm.

Because of the proximity of the trackers to the muon beam, they will lie within a region of varying magnetic field. The radial field of the trackers rises from 0 Tesla at the outer ends to roughly .3 Tesla at the inner top and bottom ends, and the vertical field drops approximately 50% from the storage dipole field of 1.451 Tesla. Shown in Figures 4·3 and 4·4 is the location of the tracker with respect to the horizontal

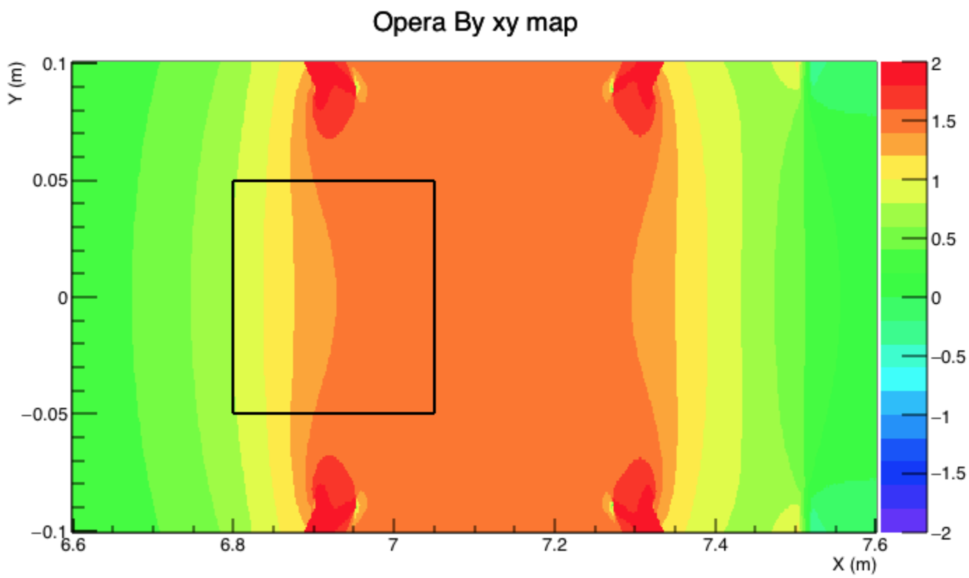


Figure 4·3: Shown is the vertical field of the $g-2$ magnet in and around the storage region as calculated in Opera 2D. The center of the storage region lies at 7.112 m along the x axis. The black box shows the rough location of the tracker with respect to the field (size exaggerated slightly). It can be seen that there is a large inhomogeneity within the tracker space, goring from left to right.

and vertical fields respectively. These large field gradients over the tracking detector region and the long extrapolation distance back to the muon decay point are special to Muon $g-2$. This is one of the main motivations for using the Geane fitting algorithm and routines, which has direct access to the field.

### 4.3.1 Track Fitting Formalism

I recommend reading [25], Chapter 4 of [26], and [27] in order to best understand the fitting algorithm. However, due to the at times confusing notation, ommitted equations or concepts, and differences between papers, I have attempted to summarize here the different sources and present the material in a more understandable and readable format. The implementation of the fitting algorithm into the code follows this section.

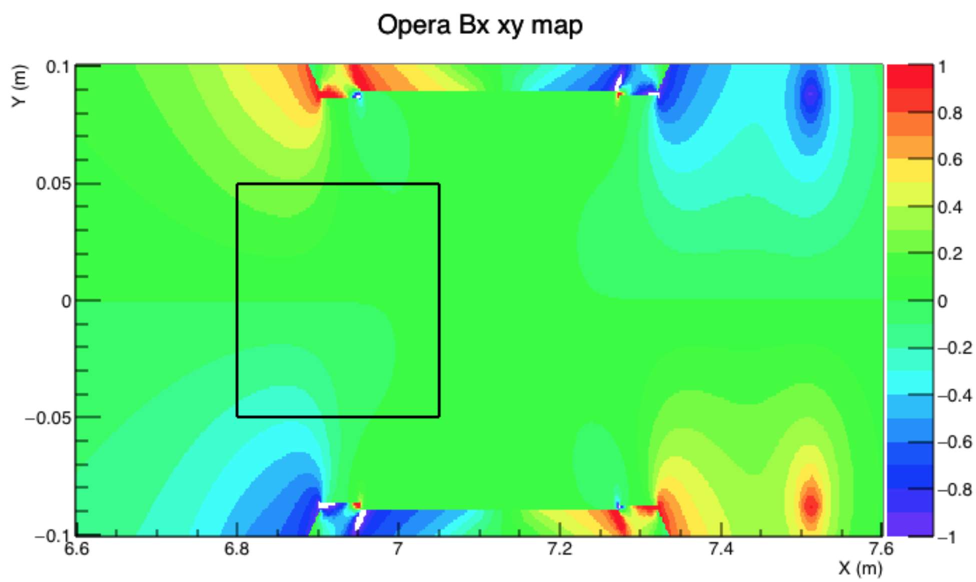


Figure 4·4: Shown is the radial field of the $g-2$ magnet in and around the storage region as calculated in Opera 2D. The center of the storage region lies at 7.112 m along the x axis. The black box shows the rough location of the tracker with respect to the field (size exaggerated slightly). It can be seen that there is a large homogeneity at the inner upper and lower ends compared to the right center. The shape of the pole pieces and tips can readily be seen.

One can define a $\chi^2$ for a track in the usual way by dividing the residuals of measured and predicted track parameters by their errors:

$$\chi^2 = (\vec{p} - \vec{x})^T (\sigma^{-1})(\vec{p} - \vec{x}), \tag{4.1}$$

where $\vec{p}$ are predicted track parameters from a fit to the measured track parameters $\vec{x}$, and $\sigma$ is a covariance matrix of errors on the fitted parameters. The Geant4 error propagation routines can be used to determine these predicted parameters and error matrices by propagating track parameters from some initial guesses. By minimizing this $\chi^2$ with respect to the track parameters one can then fit and improve the track. The Geant4 error propagation routines propagate particles along their average trajectories neglecting the effects of discrete processes, using a helix equation along small enough steps where the change in the magnetic field is small. The predicted parameters are then a function of path length:

$$p_l = F_{l,l_0}(p_0), \tag{4.2}$$

where the path length can be defined how one wishes. In our system we have tracker planes defined at X positions, and limit path lengths to reach those planes. (From here on the dependence on path length or X position will be neglected, in favor of using plane indices.) In tandem, error matrices describing the expected distribution in true parameters about those predicted parameters due to said discrete process are also calculated:

$$\sigma^{ij} =< p^i p^j > - < p^i > \cdot < p^j >, \tag{4.3}$$

where i and j are track parameter indices. These parameter vectors are 5x1 objects defined in some track representation, as described in the Coordinate Systems section. The propagation of these parameters and error matrices are done using transport matrices, which express the infinitesimal changes in parameters at some plane (or path length) with respect to the parameters at some previous plane (or previous path length):

$$\delta p_N = T_{N,N-1}\delta p_{N-1}, \tag{4.4}$$

$$\sigma_N = T_{N,N-1}\sigma_{N-1}T^T_{N,N-1}. \tag{4.5}$$

Said transport and error matrices are 5x5 objects since the parameter vectors are 5x1 objects as described above. The calculation of these transport matrices, as well as details on the functional form of 4.2 are shown in [28].

With parameters defined on such planes, one can define the $\chi^2$ as:

$$\chi^2 = \sum_{i=1}^{N}[(p_i(p) - x_i)^T(\sigma_i^{-1})(p_i(p) - x_i)], \tag{4.6}$$

where $p_i$ are the average predicted parameters from some general starting parameters $p$. At first order one can solely include the measurement errors on parameters, which fill in the diagonals of $\sigma_i$, if random processes can be neglected. Unmeasured parameters should have measurement errors of infinity (or some large value) along the diagonals in the code, which account for the fact that residuals for unmeasured parameters do not exist. When the error matrix is inverted all rows and columns of the matrix with these large numbers will fall to 0 in the $\chi^2$.

In order to get the best fit track, the $\chi^2$ should be minimized with respect to the initial track parameters p, and evaluated at some chosen or fitted parameters:

$$\frac{\partial\chi^2}{\partial p}|_{p=p'_0} = 0, \tag{4.7}$$

resulting in

$$\begin{aligned} 0 = \sum_{i=1}^{N} [ ( \frac{\partial p_i(p)}{\partial p} |_{p=p_0'} )^T (\sigma_i^{-1}) (p_i(p_0') - x_i) \\ + (p_i(p_0') - x_i)^T \frac{\partial(\sigma_i^{-1})}{\partial p} |_{p=p_0'} (p_i(p_0') - x_i) \\ + (p_i(p_0') - x_i)^T (\sigma_i^{-1}) ( \frac{\partial p_i(p)}{\partial p} |_{p=p_0'} ) ] \end{aligned} \tag{4.8}$$

where the 1st and 3rd terms are identical, and the 2nd term is small if one assumes that the error matrix doesn't change much with respect to the starting parameters. (Fair since most of the error comes from measurement, and as long as the initial guess is decent enough such that the path length through material doesn't change appreciably from one iteration to the next.) This simplifies to:

$$\sum_{i=1}^{N} T_{i0}^T (\sigma_i^{-1}) (p_i(p_0') - x_i) = 0, \tag{4.9}$$

which is just the top term with

$$T_{i0} = \frac{\partial p_i(p)}{\partial p}. \tag{4.10}$$

To solve this make the substitution

$$p_i(p_0') = p_i(p_0) + \frac{\partial p_i(p_0)}{\partial p} \Delta p_0 = p_i(p_0) + T_{i0} \Delta p_0, \tag{4.11}$$

where $p_0'$ are the improved starting parameters for the next iteration calculated from the previous starting parameters $p_0$, and $\Delta p_0$ are the changes in the starting parameters to improve the track. This equation can be plugged into the above if one makes the assumption that $T_{i0}$ does not change much from one iteration the next, which follows from the inherent nature of making small adjustments to the track in order to improve it.

After simplifying one arrives at

$$\Delta p_0 = \sigma_{p_0} \sum_{i=1}^{N} T_{i0}^{T} (\sigma_i^{-1})(x_i - p_i(p_0)), \tag{4.12}$$

where

$$\sigma_{p_0} = [\sum_{i=1}^{N} T_{i0}^{T} (\sigma_i^{-1}) T_{i0}]^{-1}, \tag{4.13}$$

is the 5x5 covariance matrix of fitted parameters on the starting plane, whose diagonals describe the errors in the 5 track parameters on that plane and in the region close to it. (The fit does not directly return fit errors for track parameters on other planes.) $\Delta p_0$ along with $\chi^2$ is exactly what we want to determine since that is what allows us to fit and improve the track from iteration to iteration.

However, since random processes should not be neglected for optimal tracking results, it makes more sense to return to the original $\chi^2$ in equation 4.1, only now the included matrix and vector objects are combined into one large linear algebra equation. Instead of a sum over N 5x1 objects multiplying 5x5 error matrices, the vectors are combined into a single 5Nx1 vector multiplying a single 5Nx5N matrix. The 5x5 diagonal blocks of this large error matrix should now include the effects due to material processes as calculated in Geant from equation 4.3 as well as the measurement errors.

Because now parameters at one plane are no longer independent of the parameters at other planes, due to correlations from these random processes, it's necessary to add off-diagonal elements into the large error matrix. These 5x5 blocks come from

$$\sigma_{MN} = T_{MN} \sigma_N, \tag{4.14}$$

for the top diagonals, and the transpose for the bottom diagaonals, where M and N are two separate planes within the detector. ($\sigma_N$ is the error matrix on plane N calculated from the starting plane.) This follows from equation 4.3 evaluated at plane M with respect to a path length from plane N, and not plane 0, which is equivalent to 4.14.

You can then minimize the $\chi^2$ in the same way, only again with the matrix objects being aggregates of the per plane objects:

$$\Delta\vec{p}_0 = \sigma_{p_0}\tau^T\sigma^{-1}(\vec{x} - \vec{p}), \tag{4.15}$$

$$\sigma_{p_0} = [\tau^T\sigma^{-1}\tau]^{-1}, \tag{4.16}$$

where $\tau$ is the combined transport matrices from the individual 5x5 matrices, a 5Nx5 object.

The unmeasured parameter errors of infinity still come into play in the final calculation in the same was as before. Because however these matrix objects are very large, and the tracking must have a certain amount of speed in order to keep up with data, it is useful to reduce the size of these matrices. (It also makes things easier programming wise. Note that there are other some other ways to speed things up, specifically the banded inversion method as described in reference [27]. This method was not used in favor of getting the code working in the simpler form in the first place, but it is a possiblity in the future to use this technique to speed things up even more.) It suffices to simply remove all rows and columns where said infinity values exist in the error matrix. This is mathematically equivalent to inverting the error matrix with the infinities included, which make all rows and columns where they exist go to zero. The associated unmeasured parameter rows in the residual vector and transport matrices must similarly be removed. This results in an Nx1 residual vector, NxN error matrix, 5xN combined transport matrix transpose, which multiply against the 5x5 covariance matrix out front to still result in a 5x1 fix to the starting parameters, and a scalar $\chi^2$ value. (Note that these element removals should be done just before the final calculation, and not higher up in the algrebra, otherwise plane correlations are not properly calculated.)

By calculating the last two equations one can fit the track, acquire a $\chi^2$ describing the degree of the fit, determine how the track parameters can be improved at the starting point, and calculate errors on those starting parameters. This algorithm can be iterated a number of times to get a best fit track until successive iterations produce no improvement, where usually 3 or 4 iterations is enough. Note that there is remarkable robustness with respect to the initial starting parameters in fitting the track. Of course if the initial starting paramaters are too poor, then the fit will not converge. All of these calculations are completed within the GeaneFitter.cc file within the framework.

## 4.4 Track Extrapolation

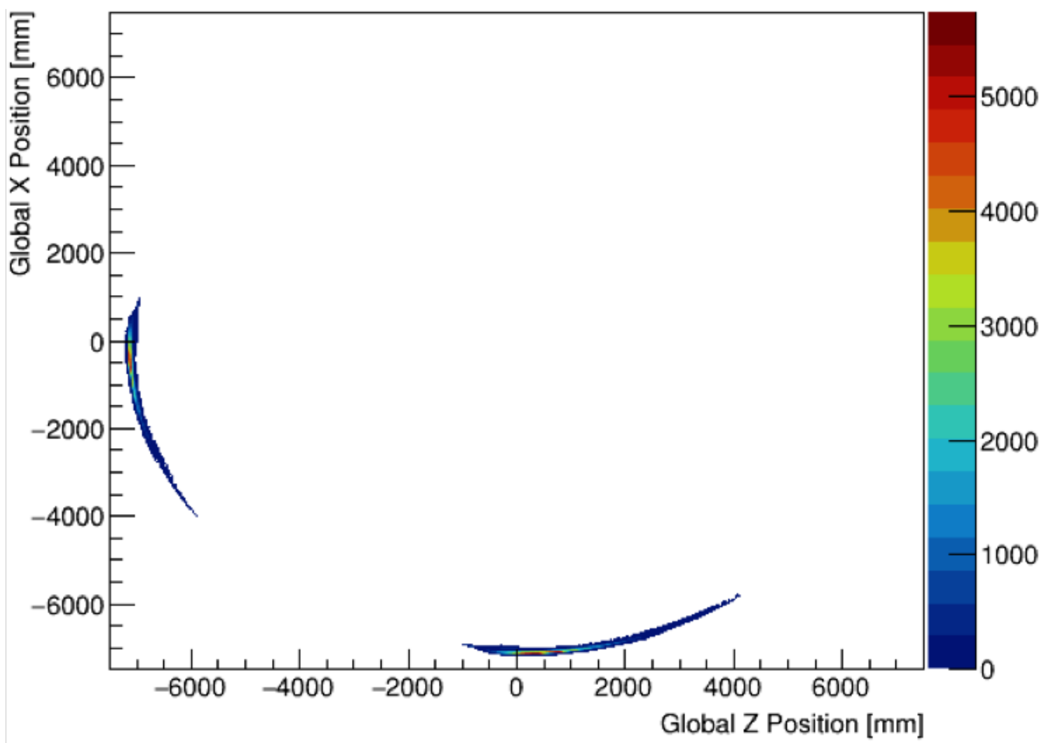


Figure 4·5: preliminary replace at some point

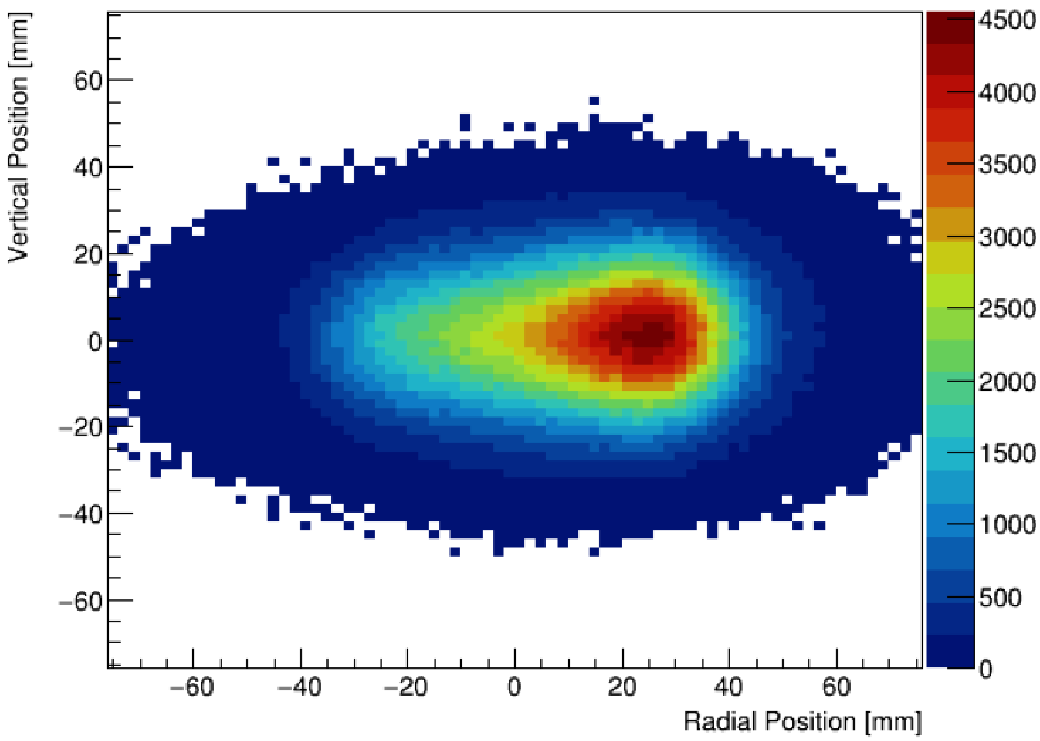


Figure 4·6: preliminary replace at some point

# Chapter 5

# $\omega_a$ Measurement

## 5.1 Data

## 5.2 Spectra Making

### 5.2.1 Clustering

### 5.2.2 Histogramming

## 5.3 Fitting

## 5.4 Systematic Errors

# Chapter 6

# Conclusion

## 6.1 Final Value

test4

# Appendix A

# $g$ for Spin-1/2 Particles and Beyond

This was taken from my old HEP2 class report paper - go back and clean this up/improve it.

The derivation contained here is taken and simplified from Reference [29]. Starting with the Dirac equation

$$(i\gamma^{\mu}\partial_{\mu} - m - e\gamma^{\mu}A_{\mu})\psi = 0 \tag{A.1}$$

and multiplying by

$$(i\gamma^{\mu}\partial_{\mu} + m - e\gamma^{\mu}A_{\mu})\psi = 0, \tag{A.2}$$

where the sign on m is reversed, you arrive at the equation

$$[(i\partial_{\mu} - eA_{\mu})(i\partial_{\nu} - eA_{\nu})\gamma^{\mu}\gamma^{\nu} - m^2]\psi = 0. \tag{A.3}$$

This can be split this into its symmetric and antisymmetric parts:

$$\begin{aligned} &(\frac{1}{4}\{i\partial_{\mu} - eA_{\mu}, i\partial_{\nu} - eA_{\nu}\}\{\gamma^{\mu}, \gamma^{\nu}\} \\ &+\frac{1}{4}[i\partial_{\mu} - eA_{\mu}, i\partial_{\nu} - eA_{\nu}][\gamma^{\mu}, \gamma^{\nu}] - m^2)\psi = 0 \end{aligned} \tag{A.4}$$

Using the identities

$$\frac{i}{2}[\gamma^{\mu}, \gamma^{\nu}] = \sigma^{\mu\nu} \tag{A.5}$$

and

$$[i\partial_\mu - eA_\mu, i\partial_\nu - eA_\nu]$$
$$= -ie[\partial_\mu A_\nu - \partial_\nu A_\nu] = -ieF_{\mu\nu} \tag{A.6}$$

where $\sigma^{\mu\nu}$ is related to the spin of the particle and $F_{\mu\nu}$ is the electromagnetic field tensor, one arrives at the form

$$((i\partial_\mu - eA_\mu)^2 - \frac{e}{2}F_{\mu\nu}\sigma^{\mu\nu} - m^2)\psi = 0. \tag{A.7}$$

Expanding out the tensor objects

$$\frac{e}{2}F_{\mu\nu}\sigma^{\mu\nu} = -e\begin{pmatrix}(\vec{B}+i\vec{E})\cdot\vec{\sigma} & \\ & (\vec{B}-i\vec{E})\cdot\vec{\sigma}\end{pmatrix} \tag{A.8}$$

and forming a new covariant derivative

$$\not{D}^2 = D_\mu^2 + \frac{e}{2}F_{\mu\nu}\sigma^{\mu\nu} \tag{A.9}$$

where $D_\mu^2$ is your ordinary covariant derivative, by moving to momentum space you can arrive at the equation

$$\frac{(H+eA)^2}{2m}\psi = (\frac{m}{2} + \frac{(\vec{p}+e\vec{A})^2}{2m} - 2\frac{e}{2m}\vec{B}\cdot\vec{s} \pm i\frac{e}{m}\vec{E}\cdot\vec{s})\psi. \tag{A.10}$$

Lo and behold, you have arrived at the Dirac g = 2 result, contained in front of the magnetic piece in the form of Equation **??**.

How then does such a term change at loop level? Most generally the vertex of a particle interacting with a magnetic field through the mediation of a photon can be represented by

$$iM^\mu = \bar{u}(q_2)(f_1\gamma^\mu + f_2p^\mu + f_3q_1^\mu + f_4q_2^\mu)u(q_1) \tag{A.11}$$

where $q_1$ and $q_2$ are the ingoing and outgoing four-momenta respectively, which can be constrained on-shell, and p is the four-momenta of the photon, which is off-shell. The $f_i$ are in general contractions of four-momenta and gamma matrices. By using the Gordon identity

$$\begin{aligned} &\bar{u}(q_2)(q_1^\mu + q_2^\mu)u(q_1) \\ &= (2m)\bar{u}(q_2)\gamma^\mu u(q_1) + i\bar{u}(q_2)\sigma^{\mu\nu}(q_1^\nu - q_2^\nu)u(q_1) \end{aligned} \tag{A.12}$$

any Feynman diagram can be reorganized into the form

$$iM^\mu = (-ie)\bar{u}[F_1(\frac{p^2}{m^2})\gamma^\mu + \frac{i\sigma^{\mu\nu}}{2m}p_\nu F_2(\frac{p^2}{m^2})]u, \tag{A.13}$$

where $F_1$ and $F_2$ are form factors. One notices that the $F_2$ piece is reminiscent of our magnetic dipole moment form that we derived from the Dirac equation. So the problem now becomes for any Feynman diagram calculation in any theory, at any order, to solve for this $F_2$ to determine the contribution to the magnetic dipole moment.

# Appendix B

# Ratio Method Derivation

## B.1 Ratio Form and Function

Consider the 5 parameter function:

$$N_5(t) = N_0 e^{-t/\tau}(1 + A\cos(\omega_a t + \phi)), \tag{B.1}$$

which describes some ideal dataset in histogram format. Here $\phi$ will be set to zero for simplicity. Now define the variables $u_+(t)$, $u_-(t)$, $v_1(t)$, and $v_2(t)$ as

$$\begin{aligned} u_+(t) &= \frac{1}{4}N_5(t + T/2) \\ u_-(t) &= \frac{1}{4}N_5(t - T/2) \\ v_1(t) &= \frac{1}{4}N_5(t) \\ v_2(t) &= \frac{1}{4}N_5(t), \end{aligned} \tag{B.2}$$

where the 1/4 out front reflects randomly splitting the whole dataset into 4 equally weighted sub-datasets, and T is the g-2 period known to high precision, $\mathcal{O}(10^{-6})$. This corresponds to a weighting of 1:1:1:1 between the datasets. To be explicit here regarding the signs, the counts that are filled into the histogram described by $u_+$ have their times shifted as $t \to t - T/2$, which is what the function $N_5(t + T/2)$ describes, and vice versa for $u_-$. To form the ratio define the variables:

$$\begin{aligned} U(t) &= u_+(t) + u_-(t) \\ V(t) &= v_1(t) + v_2(t) \\ R(t) &= \frac{V(t) - U(t)}{V(t) + U(t)}. \end{aligned} \tag{B.3}$$

Plugging in and dividing the common terms $(N_0 e^{-t/\tau}/4)$,

$$R(t) = \frac{2(1 + A\cos(\omega_a t)) - e^{-T/2\tau}(1 + A\cos(\omega_a t + \omega_a T/2)) - e^{T/2\tau}(1 + A\cos(\omega_a t - \omega_a T/2))}{2(1 + A\cos(\omega_a t)) + e^{-T/2\tau}(1 + A\cos(\omega_a t + \omega_a T/2)) + e^{T/2\tau}(1 + A\cos(\omega_a t + \omega_a T/2))}. \tag{B.4}$$

Now set $\omega_a T/2 = \delta$, and note that T is really

$$\begin{aligned} T = T_{guess} &= \frac{2\pi}{\omega_a} + \Delta T, \\ \Delta T &= T_{guess} - T_{true}. \end{aligned} \tag{B.5}$$

Being explicit,

$$\delta = \frac{\omega_a}{2} T_{guess} = \frac{\omega_a}{2}(\frac{2\pi}{\omega_a} + \Delta T) = \pi + \pi\frac{\Delta T}{T_{true}} = \pi + \pi(\delta T), \tag{B.6}$$

and $\delta$ can be redefined as

$$\delta = \pi(\delta T), \tag{B.7}$$

by flipping the sign of any cosine terms that contain $\delta$.

Then, using the trig identity

$$\cos(a \pm b) = \cos(a)\cos(b) \mp \sin(a)\sin(b) \tag{B.8}$$

so that

$$\begin{aligned}\cos(\omega_a t \pm \delta) &= \cos(\omega_a t)\cos\delta \mp \sin(\omega_a t)\sin\delta \\ &\approx \cos(\omega_a t)(1-\delta^2) \mp \sin(\omega_a t)\delta \\ &\approx \cos(\omega_a t),\end{aligned} \tag{B.9}$$

since $\delta \sim O(10^{-5})$, the ratio becomes

$$R(t) \approx \frac{2(1 + A\cos(\omega_a t)) - (1 - A\cos(\omega_a t))(e^{-T/2\tau} + e^{T/2\tau})}{2(1 + A\cos(\omega_a t)) + (1 - A\cos(\omega_a t))(e^{-T/2\tau} + e^{T/2\tau})}. \tag{B.10}$$

Expanding

$$e^{\pm T/2\tau} = 1 \pm \frac{T}{2\tau} + \frac{1}{2}\left(\frac{T}{2\tau}\right)^2 \pm \ldots, \tag{B.11}$$

repacing and simplifying,

$$R(t) \approx \frac{A\cos(\omega_a t) - C(1 - A\cos(\omega_a t))}{1 + C(1 - A\cos(\omega_a t))}, \tag{B.12}$$

where

$$C = \frac{1}{16}\left(\frac{T}{\tau}\right)^2 \approx 2.87 * 10^{-4}. \tag{B.13}$$

Using the expansion

$$f(x) = \frac{1}{1+x} = 1 - x + x^2 - \ldots, \quad |x| < 1, \tag{B.14}$$

and since $C$ is small, the denominator can be manipulated such that

$$\begin{aligned}R(t) &\approx (A\cos(\omega_a t)) - C(1 - A\cos(\omega_a t)))(1 - C(1 - A\cos(\omega_a t))) \\ &\approx A\cos(\omega_a t) - C + CA^2\cos^2(\omega_a t),\end{aligned} \tag{B.15}$$

after dropping terms of $\mathcal{O}(C^2)$ and higher. In practice the last term is ommitted since it has a minimal effect on the fitted value of $\omega_a$ [**cite**], and one arrives at

$$R(t) \approx A\cos(\omega_a t) - C, \tag{B.16}$$

the conventional 3 parameter ratio function.

In order to avoid approximations one can instead weight the counts in the histograms as

$$u_+(t) : u_-(t) : v_1(t) : v_2(t) = e^{T/2\tau} : e^{-T/2\tau} : 1 : 1, \tag{B.17}$$

so that

$$\begin{aligned} u_+(t) &= \frac{e^{T/2\tau}}{2 + e^{T/2\tau} + e^{-T/2\tau}} N_5(t + T/2) \\ u_-(t) &= \frac{e^{-T/2\tau}}{2 + e^{T/2\tau} + e^{-T/2\tau}} N_5(t - T/2) \\ v_1(t) &= \frac{1}{2 + e^{T/2\tau} + e^{-T/2\tau}} N_5(t) \\ v_2(t) &= \frac{1}{2 + e^{T/2\tau} + e^{-T/2\tau}} N_5(t). \end{aligned} \tag{B.18}$$

(These factors out front aren't so far off from 1/4 since $e^{\pm T/2\tau} \approx e^{\pm 4.35/2*64.4} \approx 1.034, .967$.) Then instead $R(t)$ becomes

$$R(t) = \frac{2(1 + A\cos(\omega_a t)) - (1 - A\cos(\omega_a t + \delta)) - (1 - A\cos(\omega_a t - \delta))}{2(1 + A\cos(\omega_a t)) + (1 - A\cos(\omega_a t + \delta)) + (1 - A\cos(\omega_a t + \delta))}, \tag{B.19}$$

where the $e^{\pm T/2\tau}$ terms out front now cancel. Using Equation B.9 again and this time avoiding approximations in $\delta$,

$$R(t) = \frac{2A\cos(\omega_a t)(1 + \cos\delta)}{4 + 2A\cos(\omega_a t)(1 - \cos\delta)}, \tag{B.20}$$

after simplifying. In the limit that

$$\delta = \pi(\delta T) \to 0 \tag{B.21}$$

since $\delta T$ is small,

$$R(t) \approx A\cos(\omega_a t), \tag{B.22}$$

with the only approximation being made at $\mathcal{O}(\delta^2) \sim \mathcal{O}(10^{-10})$.

Finally, while the 3 parameter ratio function suffices for fits to data containing slow modulations, it does not suffice for faster oscillation features. In that case it is more useful to fit with the non-approximated or simplified version of the ratio,

$$\begin{aligned} R(t) &= \frac{v_1(t) + v_2(t) - u_+(t) - u_-(t)}{v_1(t) + v_2(t) + u_+(t) + u_-(t)}, \\ &= \frac{2f(t) - f_+(t) - f_-(t)}{2f(t) + f_+(t) + f_-(t)}, \end{aligned} \tag{B.23}$$

where

$$\begin{aligned} f(t) &= C(t)(1 + A\cos(\omega_a t + \phi)) \\ f_\pm(t) &= f(t \pm T_a/2), \end{aligned} \tag{B.24}$$

and $C(t)$ can encode any other effects in the data that need to be fitted for, such as the CBO,

$$C(t) = 1 + A_{cbo} \cdot e^{-t/\tau_{cbo}} \cdot \cos(\omega_{cbo} t + \phi_{cbo}). \tag{B.25}$$

Additionally, any other fit parameters such as $A$ or $\phi$ can be made a fuction of $t$. Using the non-approximated form for the final fit function gives greater confidence in the fit results for the high precision $\omega_a$ extraction necessary for the experimental measurement.

## B.2 Ratio Point Errors

In order to determine the errors on the points in the formed ratio, Equation B.3, we use standard error propagation:

$$\sigma_R(t)^2 = \left(\frac{\partial R(t)}{\partial V(t)}\right)^2 \delta V(t)^2 + \left(\frac{\partial R(t)}{\partial U(t)}\right)^2 \delta U(t)^2 \tag{B.26}$$

This works because $V(t)$ and $U(t)$ are statistically independent datasets. Using standard error propagation again,

$$\begin{aligned} \delta V(t)^2 &= \delta v_1(t)^2 + \delta v_2(t)^2 = v_1(t) + v_2(t) = V(t), \\ \delta U(t)^2 &= \delta u_+(t)^2 + \delta u_-(t)^2 = u_+(t) + u_-(t) = U(t). \end{aligned} \tag{B.27}$$

Calculating out and simplifying the partial derivatives, (and this time dropping the $t$'s),

$$\begin{aligned} \frac{\partial R}{\partial V} &= \frac{2U}{(V+U)^2}, \\ \frac{\partial R}{\partial U} &= \frac{-2V}{(V+U)^2}. \end{aligned} \tag{B.28}$$

Combining and simplifying, we arrive at the error formula:

$$\sigma_R^2 = \frac{4UV}{(V+U)^3} = \frac{1-R^2}{(V+U)} \tag{B.29}$$

# Appendix C

# Pileup Modified Errors

In the pileup subtraction method detailed in Section **??**, pileup events are statistically constructed and then subtracted from the data. Because of this, the errors on the bins need to be adjusted appropriately. Reference [30] describes the modified errors, but is not quite correct. Here is provided an improved calculation that I believe is easier to understand. While we are mainly interested in the errors on the histogram bins after pileup subtraction, it first helps to examine the errors of the pileup histogram itself. Here we only consider doublets.

In the aysmmetric shadow window pileup method, shadow doublets are constructed from two singlets. The pileup histogram is then filled as the sum of the doublets minus the singlets,

$$P = D - S, \tag{C.1}$$

where $D$ or $S$ are only added or subtracted when they are above some energy threshold. If the threshold is set to 0, then for every doublet one entry will be added and two will be subtracted. Since these entries are exactly correlated, the error in each time bin will be

$$\sigma_P = \sqrt{N_D}, \tag{C.2}$$

where $N_D$ is the number of doublets in that time bin. If the energy threshold is above 0, then we can determine whether the counts in the pileup histogram increase

| | $E_1 < E_{th}$ | $E_1 > E_{th}$ |
|---|---|---|
| $E_2 < E_{th}$ | $N_1(+1)$ | $N_2(0)$ |
| $E_2 > E_{th}$ | $N_3(0)$ | $N_4(-1)$ |

Table C.1: Table of doublets above threshold. Here $E_1$ and $E_2$ are the energies of the two singlets, $E_{th}$ is the energy threshold, and $N_i$ are the number of doublets above threshold for the different combinations of $E_1$ and $E_2$. ($N_1$ is assumed above threshold here.) The numbers in the parentheses indicate the number of counts gained or lost in the pileup histogram.

or decrease based on whether the singlets and doublets are above threshold or not. Table C.1 shows the different combinations of counts put into the pileup histogram. The counts that go into $P$ will be

$$\begin{aligned} P &= \sum_i N_i - \text{singlets above threshold} \\ &= (N_1 + N_2 + N_3 + N_4) - (N_2 + N_4) - (N_3 + N_4) \\ &= N_1 - N_4 \end{aligned} \tag{C.3}$$

and the errors are

$$\sigma_P = \sqrt{N_1 + N_4}. \tag{C.4}$$

This makes sense considering the cases individually. In the cases for $N_1$, you will gain a count from the doublet above threshold, and lose no counts since both singlets are below threshold. In the cases for $N_2$ and $N_3$, you will gain a count from the doublet, and lose a count from one of the singlets which is above threshold. In the cases for $N_4$, you will gain a count from the doublet and lose two counts from the singlets which are both above threshold. Since the doublet and singlets are exactly correlated, the $N_1$ and $N_4$ cases naturally result in a single weight being added into the error, while the $N_2$ and $N_3$ cases result in no additions to the error.

Now what about the pileup subtracted time spectrum? Our corrected spectrum can be written as

$$N_{\text{corrected}} = N_{\text{measured}} - P. \tag{C.5}$$

What is in $N_{\text{measured}}$ doesn't matter exactly. What we care about is what is in $N_{\text{measured}}$ that is also within $P$, for that is where the correlations come from. Since $N_{\text{measured}}$ is the sum of all singlets above threshold, we can write it as

$$N_{\text{measured}} = N_{\text{other}} + N_2 + N_3 + 2N_4 \tag{C.6}$$

since we know that those cases $N_i$ listed come from singlets above threshold, and $N_{\text{other}}$ is anything in the measured hits that was not included in the pileup shadow construction. We can then replace $P$ and simplify to get

$$N_{\text{corrected}} = N_{\text{other}} - N_1 + N_2 + N_3 + 3N_4. \tag{C.7}$$

The error on the corrected histogram is then

$$\sigma_{N_{\text{corrected}}} = \sqrt{N_{\text{other}} + N_1 + N_2 + N_3 + 9N_4}. \tag{C.8}$$

Replacing $N_{\text{other}}$ as

$$N_{\text{other}} = N_{\text{corrected}} + N_1 - N_2 - N_3 - 3N_4, \tag{C.9}$$

we can remove the dependence of the corrected histogram errors on the unknown quantity and arrive at

$$\begin{aligned} \sigma_{N_{\text{corrected}}} &= \sqrt{N_{\text{corrected}} + 2N_1 + 6N_4}, \\ &= \sqrt{N_{\text{corrected}}} \cdot \sqrt{1 + (2N_1 + 6N_4)/N_{\text{corrected}}}. \end{aligned} \tag{C.10}$$

(This argument might seem circular at the end, but it works because of the squaring that occurs when calculating the error.) In the end we have a form for the bin errors of the pileup corrected histogram which only depend on $N_1$ and $N_4$ in addition to the number of counts in the corrected histogram. As shown it can be refactored into a form equal to the naive errors (just the bin content) times some correction factor. Since $N_1$ and $N_4$ are much smaller than $N_{\text{corrected}}$ at all times, and because they decay away at about twice the rate as the pileup diminishes, the change to the errors is small, of the order 1 or 2% at 30 µs.

## C.1 For the ratio function

Equation C.10 applies to the corrected errors for a pileup subtracted histogram, but what about the modifications to the ratio errors? If we parameterize that equation as

$$\sigma_{N_{\text{corrected}}} = \sqrt{N_{\text{corrected}}} \cdot \sqrt{\gamma(t)}, \tag{C.11}$$

where the correction factor $\gamma(t) \approx \gamma e^{-t/\tau_\mu}$ is small and decays at approximately the muon lifetime, we can recast the errors on the individual ratio sub-datasets as

$$\begin{aligned}
\delta V(t)^2 &= \delta v_1(t)^2 \cdot \gamma(t) + \delta v_2(t)^2 \cdot \gamma(t) = (v_1(t) + v_2(t)) \cdot \gamma(t) = V(t) \cdot \gamma(t), \\
\delta U(t)^2 &= \delta u_+(t)^2 \cdot \gamma(t + T/2) + \delta u_-(t)^2 \cdot \gamma(t - T/2) \\
&\approx u_+(t) \cdot \gamma(t) e^{-T/2\tau} + u_-(t) \cdot \gamma(t) e^{+T/2\tau} \\
&\approx (u_+(t) + u_-(t)) \cdot \gamma(t) \cdot \left(1 + \frac{1}{2}\left(\frac{T}{2\tau}\right)^2\right) \\
&\approx U(t) \cdot \gamma(t),
\end{aligned} \tag{C.12}$$

where in the last step the $\frac{1}{2}\left(\frac{T}{2\tau}\right)^2$ term has been neglected because it's small. With these approximations having been made, the modified errors on the ratio points simply become

$$\sigma_R^2 \rightarrow \sigma_R^2 \cdot \gamma(t), \tag{C.13}$$

with the correction being the same as that on the pileup subtracted histogram. Credit to Reference [31] for this derivation.

# Bibliography


[1] P. Dirac. "The quantum theory of the electron". In: *Proceedings of the Royal Society of London* Series A, Containing Papers of a Mathematical and Physical Character (1928).

[2] J. E. Nafe, E. B. Nelson, and I. I. Rabi. "The Hyperfine Structure of Atomic Hydrogen and Deuterium". In: *Phys. Rev.* 71 (12 June 1947), pp. 914–915. DOI: 10.1103/PhysRev.71.914. URL: https://link.aps.org/doi/10.1103/PhysRev.71.914.

[3] Julian Schwinger. "On Quantum-Electrodynamics and the Magnetic Moment of the Electron". In: *Phys. Rev.* 73 (4 Feb. 1948), pp. 416–417. DOI: 10.1103/PhysRev.73.416. URL: https://link.aps.org/doi/10.1103/PhysRev.73.416.

[4] Tatsumi Aoyama et al. "Complete Tenth-Order QED Contribution to the Muon g-2". In: *Phys. Rev. Lett.* 109 (2012), p. 111808. DOI: 10.1103/PhysRevLett.109.111808. arXiv: 1205.5370 [hep-ph].

[5] Tatsumi Aoyama, Toichiro Kinoshita, and Makiko Nio. "Revised and Improved Value of the QED Tenth-Order Electron Anomalous Magnetic Moment". In: *Phys. Rev.* D97.3 (2018), p. 036001. DOI: 10.1103/PhysRevD.97.036001. arXiv: 1712.06060 [hep-ph].

[6] Joshua Ellis. "TikZ-Feynman: Feynman diagrams with TikZ". In: *Comput. Phys. Commun.* 210 (2017), pp. 103–123. DOI: 10.1016/j.cpc.2016.08.019. arXiv: 1601.05437 [hep-ph].

[7] Max Dohse. "TikZ-FeynHand: Basic User Guide". In: (2018). arXiv: 1802.00689 [cs.OH].

[8] C. Gnendiger, D. Stöckinger, and H. Stöckinger-Kim. "The electroweak contributions to $(g-2)_\mu$ after the Higgs boson mass measurement". In: *Phys. Rev.* D88 (2013), p. 053005. DOI: 10.1103/PhysRevD.88.053005. arXiv: 1306.5546 [hep-ph].

[9] Tadashi Ishikawa, Nobuya Nakazawa, and Yoshiaki Yasui. "Numerical calculation of the full two-loop electroweak corrections to muon (g-2)". In: (2018). arXiv: 1810.13445 [hep-ph].

[10] F. Jegerlehner. *The Anomalous Magnetic Moment of the Muon.* Springer Tracts in Modern Physics. Springer Berlin Heidelberg, 2007. ISBN: 9783540726340. URL: https://books.google.com/books?id=uxQj004Py6AC.

[11] D. Babusci et al. "Precision measurement of $\sigma(e^+e^- \to \pi^+\pi^-\gamma)/\sigma(e^+e^- \to \mu^+\mu^-\gamma)$ and determination of the $\pi^+\pi^-$ contribution to the muon anomaly with the KLOE detector". In: *Phys. Lett.* B720 (2013), pp. 336–343. DOI: 10.1016/j.physletb.2013.02.029. arXiv: 1212.4524 [hep-ex].

[12] T. Xiao et al. "Precision Measurement of the Hadronic Contribution to the Muon Anomalous Magnetic Moment". In: *Phys. Rev.* D97.3 (2018), p. 032012. DOI: 10.1103/PhysRevD.97.032012. arXiv: 1712.04530 [hep-ex].

[13] Bogdan Malaescu. "Measurement of hadronic cross sections at BABAR with ISR and implications for the muon (g-2)". In: *Proceedings, International Conference on the Structure and the Interactions of the Photon including the 20th International Workshop on Photon-Photon Collisions and the International Workshop on High Energy Photon Linear Colliders, PHOTON 2013: Paris, France, May 20-24, 2013*. 2014. arXiv: 1404.6887 [hep-ex]. URL: http://www-public.slac.stanford.edu/sciDoc/docMeta.aspx?slacPubNumber=SLAC-PUB-16106.

[14] M. Ablikim et al. "Measurement of the $e^+e^- \to \pi^+\pi^-$ cross section between 600 and 900 MeV using initial state radiation". In: *Phys. Lett.* B753 (2016), pp. 629–638. DOI: 10.1016/j.physletb.2015.11.043. arXiv: 1507.08188 [hep-ex].

[15] Alexander Keshavarzi, Daisuke Nomura, and Thomas Teubner. "Muon $g-2$ and $\alpha(M_Z^2)$: a new data-based analysis". In: *Phys. Rev.* D97.11 (2018), p. 114025. DOI: 10.1103/PhysRevD.97.114025. arXiv: 1802.02995 [hep-ph].

[16] Michel Davier et al. "Reevaluation of the hadronic vacuum polarisation contributions to the Standard Model predictions of the muon $g-2$ and $\alpha(m_Z^2)$ using newest hadronic cross-section data". In: *Eur. Phys. J.* C77.12 (2017), p. 827. DOI: 10.1140/epjc/s10052-017-5161-6. arXiv: 1706.09436 [hep-ph].

[17] T. Blum et al. "Calculation of the Hadronic Vacuum Polarization Contribution to the Muon Anomalous Magnetic Moment". In: *Phys. Rev. Lett.* 121 (2 July 2018), p. 022003. DOI: 10.1103/PhysRevLett.121.022003. URL: https://link.aps.org/doi/10.1103/PhysRevLett.121.022003.

[18] Nils Asmussen et al. "Hadronic light-by-light scattering in the anomalous magnetic moment of the muon". In: *15th International Workshop on Tau Lepton Physics (TAU2018) Amsterdam, Netherlands, September 24-28, 2018*. 2018. arXiv: 1811.08320 [hep-lat].

[19] B. Lee Roberts. "The History of the Muon $(g-2)$ Experiments". In: *15th International Workshop on Tau Lepton Physics (TAU2018) Amsterdam, Netherlands, September 24-28, 2018*. 2018. arXiv: 1811.06974 [hep-ex].

[20] G. W. Bennett et al. "Final Report of the Muon E821 Anomalous Magnetic Moment Measurement at BNL". In: *Phys. Rev.* D73 (2006), p. 072003. DOI: 10.1103/PhysRevD.73.072003. arXiv: hep-ex/0602035 [hep-ex].

[21] D. Hanneke, S. Fogwell, and G. Gabrielse. “New Measurement of the Electron Magnetic Moment and the Fine Structure Constant”. In: *Phys. Rev. Lett.* 100 (2008), p. 120801. DOI: 10.1103/PhysRevLett.100.120801. arXiv: 0801.1134 [physics.atom-ph].

[22] J. Jackson. *Classical Electrodynamics*. Wiley Indiana, 2011.

[23] E. D. Commins and P. H. Bucksbaum. *Weak interactions of leptons and quarks*. Cambridge University Press, 1983.

[24] Diktys Stratakis et al. “Accelerator performance analysis of the Fermilab Muon Campus”. In: *Phys. Rev. Accel. Beams* 20.11 (2017), p. 111003. DOI: 10.1103/PhysRevAccelBeams.20.111003. arXiv: 1803.00597 [physics.acc-ph].

[25] V. Innocente, M. Maire, and E. Nagy. “GEANE: Average tracking and error propagation package”. In: *MC 91: Detector and event simulation in high-energy physics. Proceedings, Workshop, Amsterdam, Netherlands, April 8-12, 1991.* 1991, pp. 58–78. URL: http://innocentonnice.web.cern.ch/innocentonnice/napoli99/geane_manual.ps.

[26] Lia Lavezzi. “The fit of nuclear tracks in high precision spectroscopy experiments”. pp. 57-86. PhD thesis. Pavia U., 2007. URL: http://bamboo.pv.infn.it/doc/L_Lavezzi.pdf.

[27] V. Innocente and E. Nagy. “Trajectory fit in presence of dense materials”. In: *Nucl. Instrum. Meth.* A324 (1993), pp. 297–306. DOI: 10.1016/0168-9002(93)90992-Q.

[28] A. Strandlie and W. Wittek. “Derivation of Jacobians for the propagation of covariance matrices of track parameters in homogeneous magnetic fields”. In: *Nucl. Instrum. Meth.* A566 (2006), pp. 687–698.

[29] M. Schwartz. *Quantum Field Theory and the Standard Model*. Cambridge University Press, 2014.

[30] F. Farley et al. *Estimation of Error in Differential Pileup Subtracted Data*. E821 Muon g-2 Note 377. 2018.

[31] J. Paley. “Measurement of the Anomalous Magnetic Moment of the Negative Muon to 0.7 Parts Per Million”. PhD thesis. Boston University, 2004.

# CURRICULUM VITAE

## Joe Graduate

Basically, this needs to be worked out by each individual, however the same format, margins, typeface, and type size must be used as in the rest of the dissertation.